A global monthly field of seawater pH over 3 decades: a machine learning approach

Guorong Zhong[1,2,3,4], Xuegang Li[1,2,3,4*], Jinming Song[1,2,3,4*], Baoxiao Qu[1,2,3,4], Fan Wang[1,2,3,4], Yanjun Wang[1,4], Bin Zhang[1,4], Lijing Cheng[4,5], Jun Ma[1,2,3,4], Huamao Yuan[1,2,3,4], Liqin Duan[1,2,3,4], Ning Li[1,2,3,4],
5   Qidong Wang[1,2,3,4], Jianwei Xing[1,2,3,4], Jiajia Dai[1,2,3,4]

[1]Institute of Oceanology, Chinese Academy of Sciences, Qingdao 266071, China
[2]Laboratory for Marine Ecology and Environmental Science, Qingdao National Laboratory for Marine Science and Technology, Qingdao, China
[3]University of Chinese Academy of Sciences, Beijing 101407, China
10   [4]Center for Ocean Mega-Science, Chinese Academy of Sciences, Qingdao 266071, China
[5]Institute of Atmospheric Physics, Chinese Academy of Sciences, Beijing 100029, China

Correspondence to: Xuegang Li (lixuegang@qdio.ac.cn) and Jinming Song (jmsong@qdio.ac.cn)

Abstract. The continuous uptake of anthropogenic CO_2 by the ocean leads to ocean acidification, which is an ongoing threat to the marine ecosystem. The ocean acidification rate was globally documented in the surface ocean but limited below the
15   surface. Here, we present a monthly four-dimensional 1°×1° gridded product of global seawater pH, derived from a machine learning algorithm trained on pH observations at total scale and in-situ temperature from the Global Ocean Data Analysis Project (GLODAP). The constructed pH product covers the years 1992-2020 and depths from the surface to 2 km on 41 levels. Three types of machine learning algorithms were used in the pH product construction, including self-organizing map neural networks for region dividing, a stepwise algorithm for predictor selection, and feed-forward neural networks (FFNN) for non-
20   linear relationship regression. The performance of the machine learning algorithm was validated using real observations by a cross validation method, where four repeating iterations were carried out with 25% varied observations for each evaluation and 75% for training. The constructed pH product is evaluated through comparisons to time series observations and the GLODAP pH climatology. The overall root mean square error between the FFNN constructed pH and the GLODAP measurements is 0.028, ranging from 0.044 in the surface to 0.013 at 2000 m. The pH product is distributed through the data
25   repository of the Marine Science Data Center of the Chinese Academy of Sciences at http://dx.doi.org/10.12157/IOCAS.20230720.001 (Zhong et al., 2023).

1 Introduction

Since the Industrial Revolution, the oceans have absorbed approximately one-quarter of the carbon dioxide emitted by human activities (Le Quéré et al., 2010; Friedlingstein et al., 2023). The continuous absorption of carbon dioxide from the
30   atmosphere results in a decline in carbonate saturation states and surface seawater pH, which is a phenomenon of great concern: ocean acidification (Caldeira et al., 2003; Feely et al., 2004; Orr et al., 2005; Feely et al., 2009). As one of the primary environmental challenges the ocean faces today, ocean acidification will have extensive impacts on marine organisms and the ecological environment, resulting in notable changes to the marine ecosystem. Therefore, the assessment of ocean acidification is crucial for researching the response of marine organisms to changes in seawater pH and understanding the potential future
35   changes in the capacity of the global ocean to uptake CO_2 (Sabine et al., 2010; Guallart et al., 2015).

However, acidification research is greatly limited in terms of temporal and spatial coverage due to the lack of long-term, global coverage, and continuous seawater pH measurements. Accurate seawater pH measurements are only available from select ship surveys and a limited number of time series stations in recent decades (Fay et al., 2013; Takahashi et al., 2014). Recent research using discrete ship survey measurements revealed rapid surface ocean acidification in the Arctic Ocean, with
40   some areas showing an average decreasing pH trend of -0.0086 yr^{-1} (Luo et al., 2016; Terhaar et al., 2020; Qi et al., 2022).

Both seawater pH measurements from time series stations and discrete ship surveys suggest notable regional differences in surface ocean acidification rates (Bates et al., 2014; Lauvset et al., 2015). In the Japan/East Sea, the acidification rate in the deep ocean may be faster than previously considered and even faster than in the surface ocean (Chen et al., 2017; Li et al., 2022). Meanwhile, relatively slow acidification was found in the deep Atlantic Ocean (Guallart et al., 2015), and rising pH in

45 deep waters was also reported in the North Pacific Ocean (Ishizu et al., 2021). With limited reports about acidification below the surface, the understanding of global ocean acidification rates at different depths still needs to be improved.

The lack of long-term, global coverage, and continuous seawater pH measurements makes it difficult to expand the understanding of global deep ocean acidification using classic regression methods. Recent application of machine learning methods in the global mapping of marine carbonate system variables, such as surface ocean partial pressure of CO_2 (pCO_2,

50 Landschützer et al., 2014; Chau et al., 2022; Zhong et al., 2022), DIC (Broullón et al., 2020), and alkalinity (Broullón et al., 2019; Gregor and Gruber, 2021), indicated a feasible way to construct a global gridded seawater pH dataset. Until now, there are only surface ocean gridded pH products available (Iida et al., 2021; Gregor and Gruber, 2021), derived from other carbonate system variables and the CO2SYS program (Lewis and Wallace, 1998). In this paper, we present a monthly gridded global ocean pH product covering depths of 0-2000 m from January 1992 to December 2020, using a machine learning method trained

55 on pH measurements from the Global Ocean Data Analysis Project (GLODAP) dataset (Lauvset et al., 2022). The construct pH product provides regional and global insight into ocean acidification on timescales ranging from a few years to multiple decades.

2 Methods

2.1 Data sources and processing

60 The pH measurements at total scale and in-situ temperature and pressure from the Global Ocean Data Analysis Project (GLODAP) dataset 2023 version were used for neural network training (Lauvset et al., 2022). The constructed pH product is also at total scale and in-situ temperature based on a gridded global seawater temperature product (Cheng et al., 2017). We have collected gridded products of different variables as potential pH predictors (Table 1), and the selection of these products was based on two reasons. The first reason was their potential association with physical, chemical, and biological ocean process

65 which may affect the seawater pH. Another reason was the sufficient availability in time and spatial coverage and their potential association with the unavailable interannual variability of some climatological products used. Specifically, the mixed layer depth, bathymetry, and ocean currents were related to the physical mixing of seawater and spatial distribution of pH. Sea level pressure, surface pressure, wind speed, sea surface height, surface ocean pCO_2, and dry air mixing ratio of atmospheric CO_2 were related to the CO_2 exchange across the interface. The oceanic El Nino index, Arctic Oscillation index, and Southern

70 Oscillation index may be related to pH variability over years or decades in particular regions. The total alkalinity and DIC reflect the ocean carbonate system and were generally used to calculate seawater pH indirectly. However, products with sufficient time and spatial coverage are currently not available for these two variables, so climatological products were used for better pH spatial distribution. The remote sensing products may be useful to provide extra interannual variability information from currently used climatological products, and they were also used to test the correlation with seawater pH and

75 its potential drivers. Most predictor products were obtained with a monthly and 1°×1°resolution, which can be directly used without any treatments. Differently, products with higher resolutions were integrated into the same monthly and 1°×1° resolution by averaging, before they can be used in the relationship fitting. For instance, the mixed layer depth product, originally obtained with a resolution of 0.25°×0.25°, was converted to a 1°×1° resolution by averaging 16 0.25° grids into one 1° grid. Similarly, predictor products obtained with daily or weekly resolutions were converted to the monthly resolution by

80 directly averaging all values within the same month, such as the ocean currents product.

Table 1. Data products used as pH predictors.

Predictor	Abbreviation	Data product	Reference	Resolution
Sine of latitude	sin(Lat)	-	-	-
Sine of longitude	sin(Lon)	-	-	-
Cosine of longitude	cos(Lon)	-	-	-
Number of months since January 1992	N_{mon}	-	-	-
Year	Year	-	-	-
Month	Month	-	-	-
Depth	Depth	-	-	-
Temperature and monthly anomaly	Temp, Temp$_{anom}$	IAP global ocean temperature gridded product	Cheng et al., 2016; 2017	1°, since 1940
Salinity and monthly anomaly	Sal, Sal$_{anom}$	IAP global ocean salinity gridded product	Cheng et al., 2020	1°, since 1940
Climatological total alkalinity	Alk	AT_NNGv2_climatology	Broullón et al., 2019	1°
Climatological dissolved inorganic carbon	DIC	TCO2_NNGv2LDEO_climatology	Broullón et al., 2020	1°
Climatological dissolved oxygen	DO	WOA18	Garcia et al., 2020a	1°
Climatological nitrate	Nitrate	WOA18	Garcia et al., 2020b	1°
Climatological phosphate	Phosphate	WOA18		
Climatological silicate	Silicate	WOA18		
Mixed layer depth and monthly anomaly	MLD, MLD$_{anom}$	ECCO2 cube92	Menemenlis et al., 2008	0.25°, since 1992
Sea surface height and monthly anomaly	SSH, SSH$_{anom}$	ECCO2 cube92		
W velocity of ocean currents at 5 m, 65m, 105m, 195m, and in-situ depth	W_{vel}(5m)−W_{vel}(in-situ)	ECCO2 cube92		
Sea level pressure	SLP	ERA5	Hersbach et al., 2020	1°, since 1940
Surface pressure	P_{surf}	ERA5		
dry air mixing ratio of atmospheric CO_2 and monthly anomaly	xCO_2, xCO_2 $_{anom}$	NOAA Greenhouse Gas Marine Boundary Layer Reference	Lan et al., 2023	0.25°, since 1979
Oceanic Nino Index	MEI	bi-monthly Multivariate El Niño/Southern Oscillation index	Wolter et al., 2011	since 1979
Arctic Oscillation index	AOI	Climate Prediction Center Daily Arctic Oscillation Index	CPC, 2002	since 1950
Southern Oscillation Index	SOI	Climate Prediction Center Southern Oscillation Index	CPC, 2005	since 1951
Bathymetry	Bathy	GEBCO_2022 Grid	GEBCO, 2022	15 arc-second
10 m Wind speed and monthly anomaly	Wind, Wind$_{anom}$	ERA5	Hersbach et al., 2020	1°, since 1940
Surface ocean pCO_2	pCO_2	Stepwise FFNN	Zhong et al., 2022	1°, since 1992
Climatology of Surface Ocean pCO_2	pCO_2 $_{clim}$	MPI-ULB-SOM_FFN_clim	Landschützer et al., 2020	0.25°
Chlorophyll and monthly anomaly[*]	Chl, Chl $_{anom}$	MODIS-Aqua Chlorophyll Data	NASA, 2022	9km, since 2002
Photosynthetically Available Radiation	PAR	MODIS-Aqua Photosynthetically Available Radiation Data		

Diffuse attenuation coefficient at 490 nm	KD490	MODIS-Aqua Downwelling Diffuse Attenuation Coefficient Data
Remote sensing reflectance at 412-678 nm[**]	RRS412−RRS678	MODIS-Aqua Remote-Sensing Reflectance Data
Total absorption at 412-678 nm	Ta412−Ta678	MODIS-Aqua Inherent Optical Properties Data
Total backscattering at 412-678 nm	Tb412−Tb678	MODIS-Aqua Inherent Optical Properties Data

([*]: products from Chlorophyll to Total backscattering are satellite remote sensing products;

[**]: Remote sensing reflectance, total absorption, and total backscattering both include 10 wavelengths: 412nm, 443nm, 469nm, 488nm, 531nm, 547nm, 555nm, 645nm, 667nm, and 678nm, with each wave length regard as one individual parameter.)

On the other hand, the discrete GLODAP measurements did not match the monthly 1°×1° resolution of pH predictor products. To be consistent in the temporal and spatial resolution, the discrete GLODAP measurements were also merged into a monthly and 1°×1° resolution by averaging. The vertical layer of the temperature and salinity gridded product were used as reference standards for adjusting other collected products and constructing the pH product (Cheng et al., 2016; Cheng et al., 2017; Cheng et al., 2020). These layers covered a depth range of 0-2000 m depth, with a total of 41 layers, including 0 m, 5 m, 10-100 m at 10 m intervals, 120-200 m at 20 m intervals, 250-900 m at 50 m intervals, and 1000-2000 m at 100 m intervals. Subsequently, the in-situ seawater measurements of pH, temperature, salinity, latitude, longitude, and depth from the GLODAP dataset were averaged monthly within the same 1°×1° grid (first grid centered at 89.5°S, 0.5°E) and within the same vertical layer to match the resolution of the predictor products. Since a direct average was used instead of a weighted average, the average latitude, longitude, and depth values from the initial measurements within the same 1°×1° grid were then used as new sample position for the derived monthly measurements, instead of being located at the center point of grids. The pH measurements obtained after the 1°×1° grid and monthly averaging were employed to establish a neural network model and fit a non-linear relationship with the pH predictors.

2.2 Biogeochemical province

To identify predictors that are most relevant to pH drivers in different regions, we divide the global ocean into distinct biogeochemical provinces using self-organizing map neural networks (SOM). This was achieved by inputting climatological surface seawater temperature, salinity, mixed layer depth, chlorophyll concentration, dissolved oxygen, nitrate, phosphate, silicate, and pH (Lauvset et al., 2016) into a 4×4 SOM network, resulting in the partitioning of the global ocean into preliminary 16 provinces. Subsequently, the province with fewer than ten connected grids or less than 100 GLODAP pH measurements was merged with the nearest neighboring provinces. In addition, the province separated by continents was manually subdivided into distinct provinces, such as the province spanning the North Pacific and the North Atlantic. As a result, the global ocean was divided into 14 biogeochemical provinces, as shown in Figure 1. The boundary of SOM provinces was treated with a cross-boundary method to relieve the discontinuity of spatial distribution near the SOM boundaries (Zhong et al., 2022). Due to much more dynamic variation in coastal seawater pH, the global coastal areas have higher predicting errors than the open oceans. In this study, we removed all coastal areas shallower than 200 m bathymetry. Furthermore, because the drivers of seawater pH near the surface is different with deeper waters, the ocean area was divided into two layers: the mixed layer (ranging from 0 m to mixed layer depth) and the intermediate layer (ranging from mixed layer depth to 2000 m). Consequently, the gridded product construction in each province was carried out separately for the two layers. Application of SOM method can effectively reduce regional predicting errors, but it also generates discontinuity problems near the boundary. Therefor, a cross-boundary method was used to improve the FFNN performance near the SOM and vertical boundary (Zhong et al., 2022). The spatial scale of training samples in each SOM province was expand out of the boundary for 10 grids, and out of the vertical

boundary for 2 layers (Figure 2). By increasing additional training sample outside the SOM province and vertical layer
120 boundary, the cross-boundary method can effectively reduce the appearance of dysconnectivity near boundaries (Figures S1 and S2).
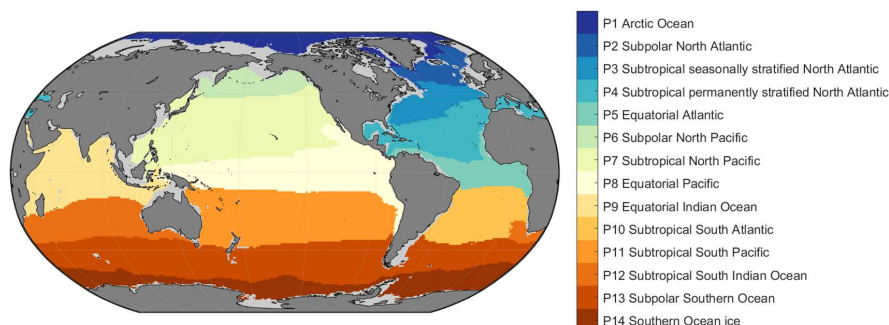
Figure 1: Map of the biogeochemical province.
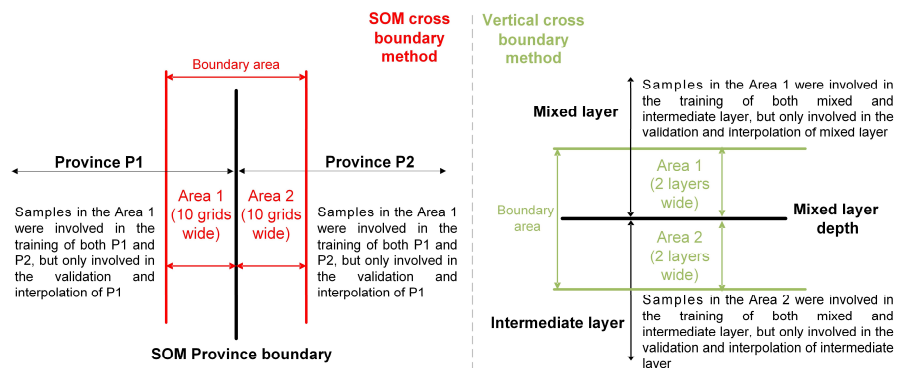
125 **Figure 2: Cross-boundary method for better connectivity near the SOM boundary and vertical boundary.**

2.3 pH product construction

The forward feedback neural network (FFNN) with a single hidden layer was applied to fit the non-linear relationship between seawater pH and its predictors to perform spatial interpolation and construct the gridded product:

$$\text{pH} = f(\text{Predictors}_1, \text{Predictors}_2, …, \text{Predictors}_N) \tag{1}$$

130 where f was a non-linear function built by FFNN, and predictors related to chemical, physical, and biological properties were selected from products in Table 1. Considering the regional difference in pH variability and its drivers, identifying the combination of most relevant predictors in each region was a critical precondition. Thus, the entire product construction method includes two steps (Figure 3):

(1) Selection of seawater pH predictors in each province using the Stepwise FFNN algorithm. All the collected products
135 were input into the Stepwise FFNN algorithm to identify the predictors that yield the lowest predicting errors for seawater pH (Zhong et al., 2022). The variation in standard deviation (MAE) calculated by the K-fold cross validation method will feed back to update the input products. The input variables are selected as pH predictors one by one in the way MAE decreases the fastest. This selection process continued until no further reduction in MAE was observed, regardless of whether a variable was added or removed. The co-correlation among pH predictors was not considered when choosing the variables in Table 1, but
140 was considered in the design of the Stepwise FFNN algorithm. Since overfitting caused by co-correlation and underfitting caused by an insufficient number of predictors both lead to a significant increase in pH predicting errors, the lowest predicting

error occurs between these two states. The Stepwise FFNN algorithm tests all products based on changes in predicting errors, to reach a balance avoiding overfitting and underfitting. Therefore, most of the co-correlation among the selected predictors has been removed in this Stepwise FFNN selection procedure. If products with co-correlations are still selected, some products

145 may provide important additional information in specific regions, leading to a greater reduction in predicting errors compared to the increase caused by overfitting. In each province, pH predictors were selected separately for the mixed layer (Table 2) and intermediate layer (Table 3). In certain polar areas and prior to August 2002 when satellite remote sensing products (products from Z_{eu} to Tb678 in Table 1) were not available, the additional selection of predictors was carried out without the use of satellite remote sensing products (Table S1). These satellite products were not used in the intermediate layer due to low

150 correlation with seawater pH, with no need for additional selection.

(2) Fitting the non-linear relationship between seawater pH and selected predictors. In each province, a group of FFNNs was trained separately for the mixed layer and intermediate layer to fit the non-linear relationship, based on the predictors selected in the first step. To mitigate the influence of the FFNN's initial state on predicting values, multiple networks with the same structure but different initial states were trained and their results were averaged. Then the seawater pH was calculated

155 using the trained FFNNs, along with the product of pH predictors. If satellite remote sensing products were used, additional FFNNs were trained with predictors in Table S1, for pH product construction in some polar areas and before August 2002 when satellite products were unavailable. Finally, the seawater pH predicting values from all FFNNs were combined to construct the global ocean 0-2000 m seawater pH gridded product from January 1992 to December 2020, with a 1°×1° spatial resolution.
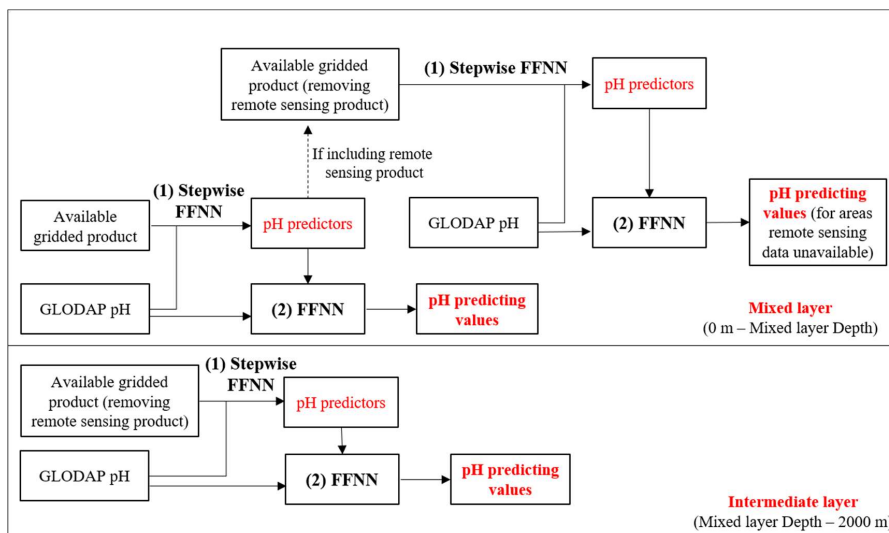
160

Figure 3: The procedure of pH product construction. (1) Stepwise FFNN: the algorithm for selecting predictors (Zhong et al., 2022); (2) FFNN: fitting the non-linear relationship between seawater pH and its predictors. Available gridded product: products listed in table 1, from which pH predictors were selected; Remote sensing products were not available in some polar areas and during the period before August 2002. Mixed layer depth: using ECCO2 cube92 mixed layer depth product (Menemenlis et al., 2008).

165

Table 2. Predictors selected by the stepwise FFNN algorithm in the Mixed layer.

Province	FFNN neurons	pH Predictor
P1 Arctic Ocean	10	$p\mathrm{CO_2}$, sin(Lat), Depth, Sal, W_{vel}(105m)
P2 Subpolar North Atlantic	10	Phosphate, DO, N_{mon}, DIC, Sal, Bathy
P3 Seasonally stratified North Atlantic	75	$p\mathrm{CO_{2\,clim}}$, Depth, Temp, Silicate, $p\mathrm{CO_2}$, DIC
P4 Permanently stratified North Atlantic	20	$p\mathrm{CO_2}$, Phosphate, sin(Lat), Depth, SSH_{anom}, Sal_{anom}, W_{vel}(195m), Temp, W_{vel}(in-situ), $p\mathrm{CO_{2\,clim}}$, DO
P5 Equatorial Atlantic	50	sin(Lat), Tb469, Temp, Tb555, Tb547, Nitrate, Tb667, Tb678, Tb488, Tb645, Tb531, Sal
P6 Subpolar North Pacific	10	DIC, sin(Lat), sin(Lon), Depth, Salinity, Temp, $p\mathrm{CO_2}$, W_{vel}(in-situ)
P7 Subtropical North Pacific	50	Temp, sin(Lon), sin(Lat), $p\mathrm{CO_2}$, Phosphate, Sal, $p\mathrm{CO_{2\,clim}}$, Depth, cos(Lon), Nitrate, Sal_{anom}, Alk
P8 Equatorial Pacific	20	$p\mathrm{CO_2}$, Silicate, Depth, Sal, Temp, Wind, Alk, RRS645, Ta555, Ta547
P9 Equatorial Indian Ocean	10	DO, $Temp_{anom}$, $p\mathrm{CO_2}$, Depth, W_{vel}(in-situ), W_{vel}(195m), W_{vel}(65m)
P10 Subtropical South Atlantic	10	$p\mathrm{CO_2}$, DIC, Silicate, RRS645, W_{vel}(in-situ), Ta547, Temp, Ta667, Sal, Phosphate, Tb412, Ta412, Tb443, DO, $x\mathrm{CO_2}$
P11 Subtropical South Pacific	10	Silicate, $p\mathrm{CO_2}$, Tb412, Phosphate, Depth, Ta488, $Temp_{anom}$, Ta531
P12 Subtropical South Indian Ocean	10	$p\mathrm{CO_2}$, Silicate, Phosphate, Nitrate, Depth, Wind
P13 Subpolar Southern Ocean	20	Phosphate, Depth, $p\mathrm{CO_2}$, $p\mathrm{CO_{2\,clim}}$, Sal, DIC, Nitrate
P14 Southern Ocean ice	20	Phosphate, Temp, $p\mathrm{CO_2}$, Depth, Sal, Alk, SSH

(The predictors are arranged in order of relative importance, with the variables listed at the front of each province being more effective in reducing predicting errors when used as pH predictors.)

Table 3. Predictors selected by the stepwise FFNN algorithm in the intermediate layer.

Province	FFNN neurons	pH Predictor
P1 Arctic Ocean	50	Phosphate, Nitrate, Sal, Depth, sin(Lat), SSH
P2 Subpolar North Atlantic	20	Phosphate, DO, Depth, Year, Sal, Temp, Nitrate, sin(Lat), Alk, W_{vel}(195m)
P3 Seasonally stratified North Atlantic	10	DIC, Nitrate, Temp, Depth, sin(Lon), Year
P4 Permanently stratified North Atlantic	20	Phosphate, Temp, Depth, sin(Lat), N_{mon}, sin(Lon), Sal, Sal_{anom}, Nitrate, W_{vel}(in-situ)
P5 Equatorial Atlantic	25	Depth, DIC, Sal, sin(Lat), Temp, Phosphate, SSH, cos(Lon), Nitrate, Silicate
P6 Subpolar North Pacific	25	Phosphate, Sal, Depth, Temp, sin(Lat), Silicate, $x\mathrm{CO_{2\,anom}}$, Alk, Nitrate
P7 Subtropical North Pacific	50	Phosphate, Sal, Temp, Silicate, N_{mon}, sin(Lat), sin(Lon), Depth, Alk, DIC, Nitrate
P8 Equatorial Pacific	25	Phosphate, Depth, Temp, sin(Lat), Sal, Silicate, $x\mathrm{CO_2}$, Nitrate, W_{vel}(105m)
P9 Equatorial Indian Ocean	10	Phosphate, Depth, $p\mathrm{CO_2}$, W_{vel}(in situ)
P10 Subtropical South Atlantic	10	Temp, DIC, Sal, Depth, Nitrate, W_{vel}(65m), $p\mathrm{CO_2}$, $p\mathrm{CO_{2\,clim}}$, DO, W_{vel}(195m)
P11 Subtropical South Pacific	25	Phosphate, Depth, Temp, $x\mathrm{CO_2}$, sin(Lat), Silicate, Sal, Alk
P12 Subtropical South Indian Ocean	25	Phosphate, $p\mathrm{CO_2}$, Depth, Temp, Sal, $p\mathrm{CO_{2\,clim}}$, Silicate, DO
P13 Subpolar Southern Ocean	50	DIC, Temp, Depth, N_{mon}, Sal, Alk, DO, Silicate, P_{surf}, $Temp_{anom}$
P14 Southern Ocean ice	25	cos(Lon), sin(Lat), Depth, DIC, Temp, Sal

170 (The predictors are arranged in order of relative importance, with the variables listed at the front of each province being more effective in reducing predicting errors when used as pH predictors.)

2.4 Validation and uncertainty

The constructed pH product was validated based on pH measurements from GLODAP and time series stations. First, the root mean square error (RMSE) between the FFNN predicting pH and GLODAP pH measurements was calculated using the

175 K-fold cross validation method. The GLODAP pH measurements were divided by years, and the K value was 4 to keep aside

25% independent measurements for testing in each one of the total 4 iterations. Thus, within every set of four consecutive years, pH measurements from three years were utilized for training the FFNN model, while the measurements from the remaining year were employed for testing. This approach ensured the independence between the training and testing groups (Gregor et al., 2019; Zhong et al., 2022). Subsequently, the pH measurements in the testing group were compared against the FFNN-predicted pH values based on the training group. A total of 4 iterations were carried out with each iteration designating different years as the testing groups, ensuring that measurements from all years have been set as the test group once and matched with a FFNN-predicted value. By comparing all FFNN-predicted pH values with GLODAP pH measurements, the RMSE of pH and $[H^+]$ was calculated to evaluate the performance of the FFNN model. The predicting of the testing group from the training group is similar to the interpolation process, wherein the FFNN is trained with existing measurements to predicting pH in unknown areas.

Second, the constructed seawater pH product was compared with independent pH measurements from the Hawaii Ocean Time-series (HOT, 22° 45' N, 158° 00' W, since October 1988) (Dore et al., 2009), Bermuda Atlantic Time-series Study (BAT, 31°50' N, 64°10' W, since October 1988) (Bates et al., 2007; Bates et al., 2020), and The European Station for Time Series in the Ocean Canary Islands (ESTOC, 29°10' N, 15°30' W, from 1995 to 2009) (González-Dávila et al., 2010). Validation based on these independent measurements from time series stations provides additional evidence of data accuracy.

A comparison between the method of training FFNN with pH and the method of training FFNN with $[H^+]$ then converting to pH was carried out, to validate which way has a lower pH predicting error. In addition, to identify the difference in pH variability uncertainty hidden by logarithm among regions with the same pH RMSE but different pH level, the uncertainty of reconstructed pH values was converted from $[H^+]$ RMSE instead of directly using pH RMSE. The pH obtained from the FFNN was first converted to $[H^+]$ to estimate RMSE. Subsequently, the pH values were shown as $pH_0 \pm \sigma$ at each given pH_0 value, and the uncertainty σ stem from FFNN predicting errors was calculated as the following:

$$\sigma = -\log_{10}(10^{-pH_0} - RMSE_{[H^+]}) - pH_0 \tag{2}$$

where $RMSE_{[H^+]}$ was the RMSE of $[H^+]$ converted from FFNN pH in each layer of all 14 biogeochemical provinces, pH_0 was the specific predicted pH value. The uncertainty σ calculated by this method is simultaneously related to the pH predicting error and pH level, which better distinguishes the differences in uncertainty across different regions. The uncertainty of products used as pH predictors is one ineluctable source for pH predicting errors of the FFNN model. However, the direct estimation of pH uncertainty from summing the uncertainty of each used product is not feasible, as the relationships between pH and predictors are not established as specific formulas but as matrix manipulations. Therefore, the uncertainty of our pH product was directly estimated from the FFNN pH predicting errors, instead of synthesizing the inherent uncertainty of each used predictor product. The inherent uncertainty and construction method of predictor products are described in the Supplementary text.

3 Results and discussion

3.1 Validation of algorithm

3.1.1 Validation based on GLODAP and time series measurements

Compared with the GLODAP dataset, most predicting values of Stepwise FFNN are close to the GLODAP pH measurements, concentrated around the y=x line (Figure 4). Only a few samples notably differ between the pH measurements and the predicting values, with the RMSE of 0.028 in the global ocean of 0-2000 m. A better performance of the FFNN was found in the intermediate layer, with testing samples more concentrated on the y=x line. The RMSE in the mixed layer is 0.034, higher than 0.026 in the intermediate layer. The minor difference between the predicting value and the pH measurements and the R^2 of 0.97 in the intermediate layer suggested a sufficient fitting ability of FFNN.
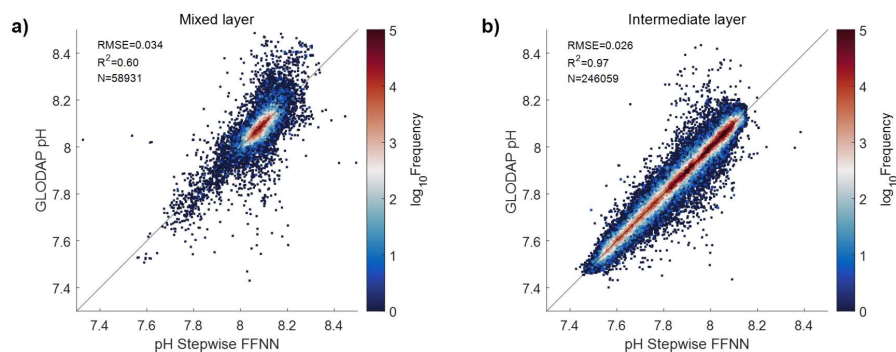
Figure 4: Comparison between FFNN predicting pH and GLODAP pH measurements. a): mixed layer from the surface to mixed layer depth; b): intermediate layer from mixed layer depth to 2000 m.

The RMSE between the FFNN predicting pH and GLODAP pH measurements at most grids were lower than 0.03 (Figure 5a). The performance of FFNN was relatively better in the temperate oceans, with the RMSE lower than 0.02 at some temperate grids. However, relatively higher RMSE was found in the equatorial and polar oceans, especially in the eastern equatorial Pacific, the near-polar North Pacific, and the northwest Indian Ocean. The RMSE was relatively lower in regions with concentrated GLODAP measurements, such as the near-polar North Atlantic, south Atlantic, and south Indian Ocean.

Due to the higher seasonal and interannual variability of seawater pH near the surface ocean, the RMSE decreases with depth in all basins (Figure 5b). At the surface ocean, the RMSE between the FFNN predicting pH and the GLODAP pH measurements was 0.044. The RMSE fluctuates between 0.032 and 0.048 at the subsurface 0-200 m. The RMSE between the FFNN predicting pH and the GLODAP pH measurements decreased rapidly from the 200 m depth. In the global ocean 1500-2000 m depth, the global RMSE was lower than 0.015. While at 2000 m depth, the global ocean RMSE at 2000m was only 0.013, with the higher RMSE in the Arctic Ocean and the lower in the Southern Ocean. The vertical distribution of the RMSE and statistical distribution of pH difference in different basins all suggested a relatively higher predicting error in the mixed layer than in the intermediate layer (Figure 5d). The vertical difference of RMSE between the mixed layer and intermediate layer was most notable in the Arctic and Indian Ocean, where the RMSE at different depths was also higher than the other basins. The RMSE in the surface Arctic Ocean was higher than 0.10 and decreased rapidly to 0.025 by 450 m depth. On the contrary, the RMSE of the surface Indian Ocean was low, only 0.018, but increased to 0.053 by 80 m depth and then decreased continuously with depth. The high RMSE of subsurface oceans is because there are almost no GLODAP pH measurements in the entire Indian Ocean at 50-150 m depth. The RMSE in different years also suggested the notable influence of pH measurement amount on the FFNN predicting errors. The RMSE in the early years was relatively higher than in recent years, while the number of GLODAP measurements increased with the years (Figure 5c).
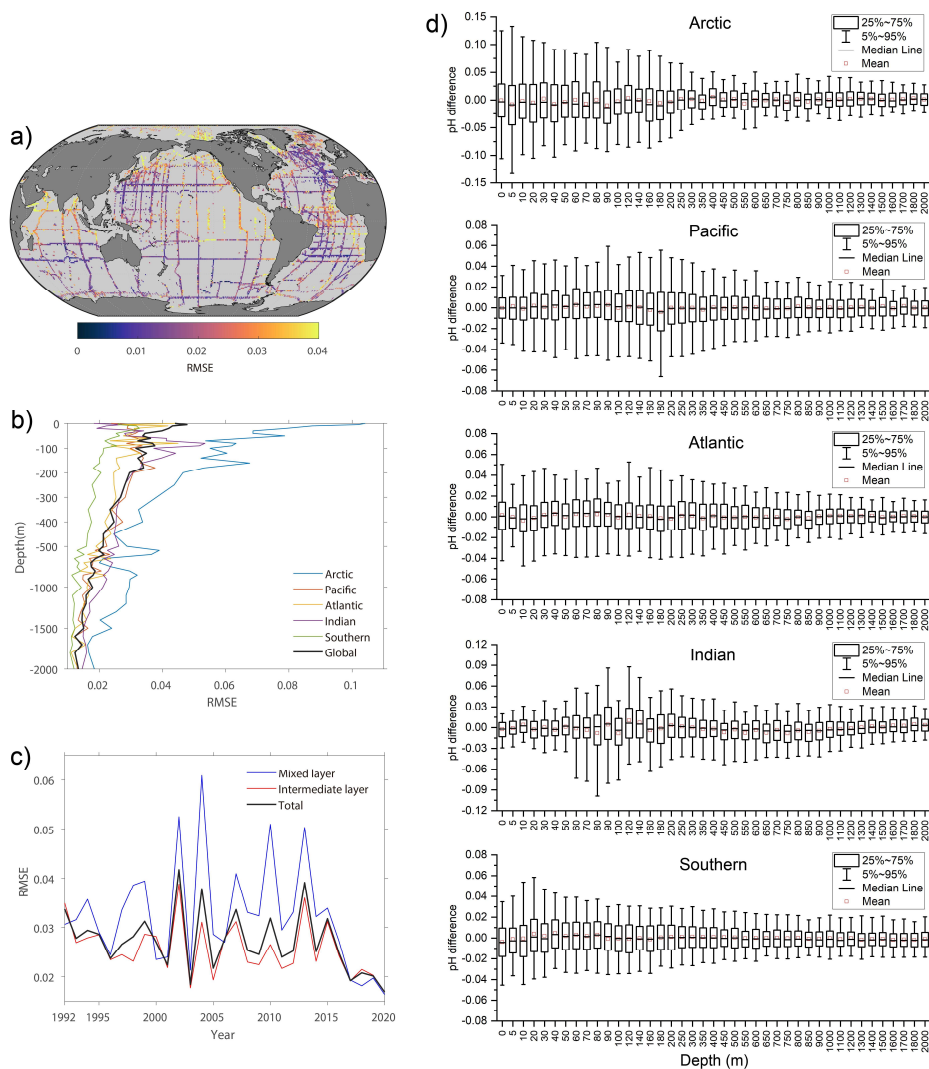
Figure 5: Distribution of RMSE between FFNN predicted pH values and GLODAP pH measurements. a): global spatial distribution of RMSE between FFNN predicted pH and GLODAP pH measurements at 0-2000 m; b): basin average RMSE at different depth; c): temporal distribution of global RMSE; d): Statistical distribution of pH difference between predicted pH values and GLODAP pH measurements in each basin
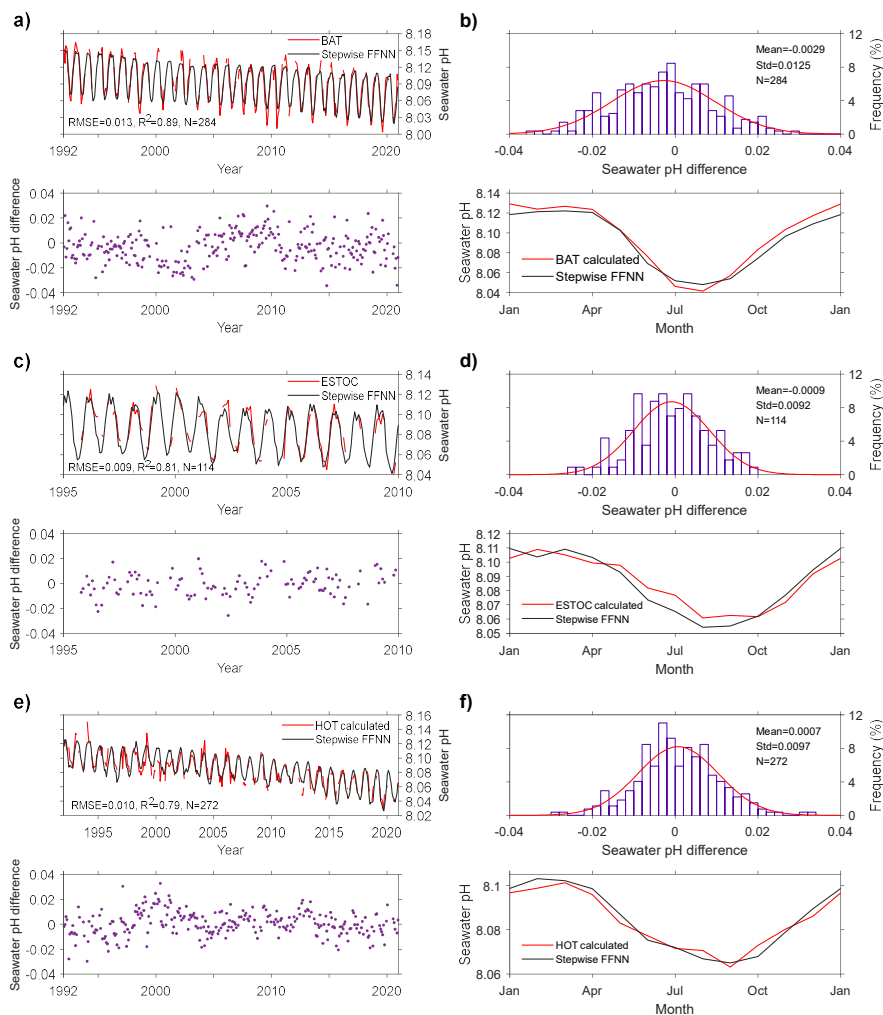
Figure 6: Comparison between FFNN predicted pH and time-series measurements. a-b): pH value, pH difference and its distribution, pH seasonal variability of FFNN result and time series measurements at the BAT station; c-d): the ESTOC station; e-f): the HOT station.

250   The Stepwise FFNN pH product showed variability of seawater pH close to the independent time series observations in the surface ocean from HOT, ESTOC, and BAT stations (Figure 6). At the BAT station, the RMSE between the constructed pH product and time series observations was only 0.013. The surface seawater pH of our Stepwise FFNN product decreased by 0.0017 ± 0.0007 yr^{-1} on average during the past three decades at the BAT station, close to the -0.0018 ± 0.0001 yr^{-1} of BAT time series observations in the same period (Bates et al., 2020). At the ESTOC station, the Stepwise FFNNN product and time series observations were also well consistent, with the RMSE of only 0.009 and a similar long-term trend (Chau et al., 2022).

255 The RMSE between the Stepwise FFNN product and HOT time series observations was also only 0.010, and the long-term trends of the Stepwise FFNN pH product was 0.0018 ± 0.0004 yr^{-1}, consistent with the HOT time series observations. Although at the BAT station, the Stepwise FFNN product suggested a smaller seasonal change scale than the time series observations, the seasonal patterns of surface seawater pH were consistent between the Stepwise FFNN product and time series observations at all three stations. Compared to previous surface ocean seawater pH product, which were derived from constructed DIC, TA,

260 or pCO$_2$ products, the Stepwise FFNN product had lowest surface RMSE at the ESTOC station, and similar RMSE values to other products at the BAT and HOT stations (Table 4). The long-term pH trend of our product differed from other gridded products at the ESTOC station, but the result is still close to the real observations.

Table 4: Comparison of surface acidification rate with previous product in different time series stations.

Seawater pH product		Station			Product coverage
		BAT	ESTOC	HOT	
Time series observation	Period	1992~2020	1995~2010	1992~2020	-
	Acidification rate (yr^{-1})	-0.0018 ± 0.0001	-0.0016 ± 0.0001	-0.0018 ± 0.0001	
Stepwise FFNN product (This study)	RMSE	0.013	0.009	0.010	Global ocean 0-2000 m
	Acidification rate (yr^{-1})	-0.0017 ± 0.0007	-0.0014 ± 0.0005	-0.0018 ± 0.0004	
JMA product (Iida et al., 2021)	RMSE	0.014	0.010	0.012	Global surface ocean
	Acidification rate (yr^{-1})	-0.0018	-0.0022	-0.0020	
CMEMS product (Chau et al., 2022)	RMSE	0.012	0.013	0.009	Global surface ocean
	Acidification rate (yr^{-1})	-0.0018	-0.0020	-0.0021	
OS-ETHZ product (Gregor et al., 2021)	RMSE	0.013	0.011	0.009	Global surface ocean
	Acidification rate (yr^{-1})	-0.0018	-0.0017	-0.0019	

265 (RMSE: root mean square error between pH products and time series observations;

Stepwise FFNN product: constructed from pH measurements with 1°×1° and monthly resolution from 1992 to 2020, covering global ocean 0-2000 m;

JMA product: constructed from DIC and Alk with a 1°×1° and monthly resolution from 1990 to 2021, covering global surface ocean;

CMEMS product: constructed from pCO$_2$ and Alk with a 1°×1° and monthly resolution from 1985 to 2021, covering global surface ocean;

270 OS-ETHZ product: constructed from pCO$_2$ and Alk with a 1°×1° and monthly resolution from 1982 to 2022, covering global surface ocean.)

3.1.2 Comparison of performance between FFNNs training based on pH and [H$^+$]

Due to the logarithmic relationship between pH value and [H$^+$] concentration, results obtained from training FFNN with pH and from training FFNN with [H$^+$] then converting outputs into pH may differ. A comparison of predicting errors was conducted between these two training methods. The results show a nearly consistent pH RMSE between the FFNN training

275 with pH and with [H$^+$] (Figure 7). As the pH measurements of all GLODAP samples are closer to a normal distribution than the [H$^+$], the predicting error was slightly lower in most regions when the FFNN was trained with pH, but the difference in predicting errors was extremely small. In addition, the FFNN trained using [H$^+$] occasionally produced negative [H$^+$] in regions with extremely low [H$^+$]. Therefore, it is better to train FFNN using pH rather than using [H$^+$] in the reconstruction process of the pH product.

280 The distribution patterns of regional pH RMSE and [H$^+$] RMSE are inconsistent whenever the FFNN was trained using pH or [H$^+$]. In fact, the pH RMSE of the intermediate layer in regions such as the subarctic North Pacific and the equatorial Pacific is significantly lower than that in the intermediate layer of the Arctic Ocean, but their [H$^+$] RMSE is higher than that of the intermediate layer in the Arctic Ocean (Figure 7a and 7b). This is caused by the effect of the logarithmic relationship. If the pH values are different for the same pH RMSE, the corresponding [H$^+$] RMSE will be different. Therefore, the uncertainty

285 of the pH product is calculated based on the [H$^+$] RMSE and pH value, rather than solely based on the pH RMSE.
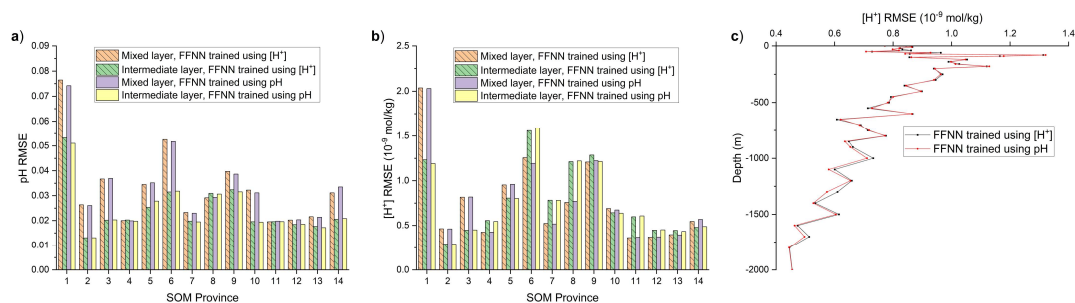
Figure 7: Comparison of pH RMSE and [H⁺] RMSE from training FFNN using pH and using [H⁺]. a): pH RMSE of FFNN trained using pH and [H⁺] in each biogeochemical province, the predicted [H⁺] from FFNN trained using [H⁺] was converted to pH for estimating pH RMSE. b): [H⁺] RMSE of FFNN trained using pH and [H⁺] in each biogeochemical province; c): [H⁺] RMSE of FFNN trained using pH and [H⁺] in each vertical layer; the predicted pH from FFNN trained using pH was converted to [H⁺] for estimating [H⁺] RMSE. The numbers shown in the X-axis represent the SOM province in Figure 1.

3.2 Gridded pH product

3.2.1 Spatial pH distribution

The spatial distribution of long-term average seawater pH in the constructed Stepwise FFNN product suggests the lowest surface seawater pH in the equatorial Pacific with an average value near 8.00 (Figure 8a), which is in good agreement with the surface seawater pH range of 7.91-8.12 observed in the equatorial Pacific in recent decades (Sutton et al., 2014). The upwelling transporting the deep water with high dissolved inorganic carbon and low pH to the surface was the main driver. The equatorial Indian Ocean and the equatorial Atlantic also show a low surface pH of about 8.05, consistent with the distribution patterns of the GLODAP pH climatology (Lauvset et al., 2016). The highest surface pH is found in the Atlantic sector of the Arctic Ocean, where the average surface pH was around 8.15 during the past three decades. Besides, the average surface pH in temperate oceans is relatively higher, such as the south Indian and south Atlantic Oceans. In the Pacific Ocean, the high surface pH is mainly concentrated in the west, while the average surface pH in the East temperate Pacific was about 8.05. At the deeper depth of 1000 m, the spatial distribution pattern of FFNN pH product is generally consistent with the GLODAP climatology, despite still some disturbance of bad FFNN performance along the SOM province boundary.

305
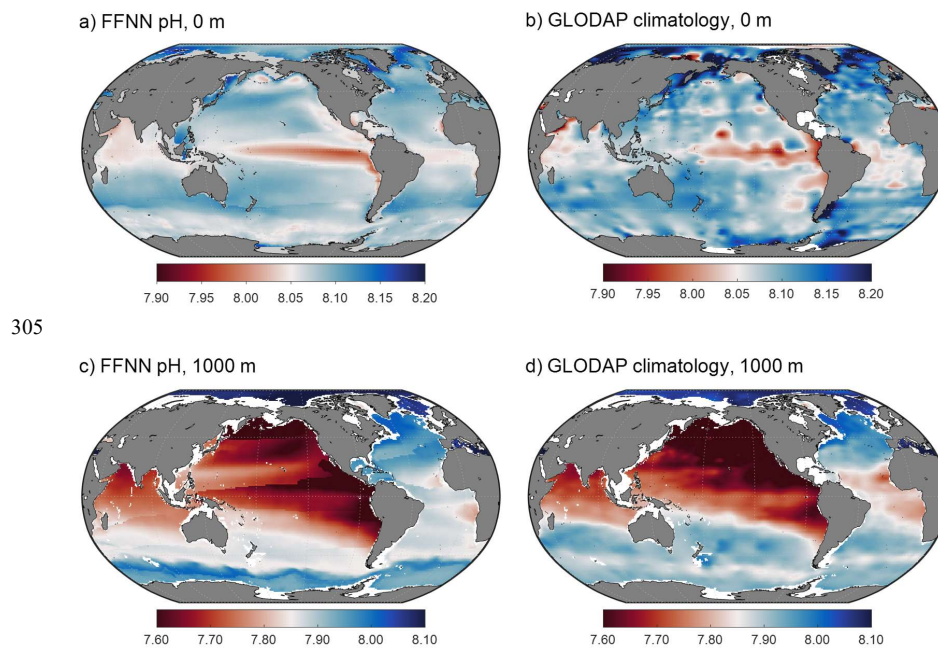
Figure 8: Average pH distribution from FFNN pH product and GLODAP climatology normalized to the year 2002. The
GLODAP climatology data is from Lauvset et al., 2016.

The vertical distribution of average pH in the constructed product showed a notable pH decrease with increasing depth in
310   the upper 500 m of different basins (Figure 9). The seawater pH was the lowest at nearly 500 m and rose with increasing depth
at 500-2000 m in the Pacific and Atlantic oceans. The distribution pattern of seawater pH in the Indian Ocean was similar to
that in the South Pacific, with the lowest seawater pH appearing near 1000 m. The subsurface seawater with low pH in the
Atlantic Ocean and Indian Ocean was mainly concentrated in the equatorial region. In contrast, subsurface seawater with low
pH in the Pacific Ocean appeared in subpolar and equatorial regions. The overall distribution pattern of the constructed pH
315   product is in good agreement with previous research (Lauvset et al., 2016; Lauvset et al., 2020). It can be concluded that the
FFNN fitted the relationship between GLODAP seawater pH and its predictors well, and the constructed pH product has good
accuracy.
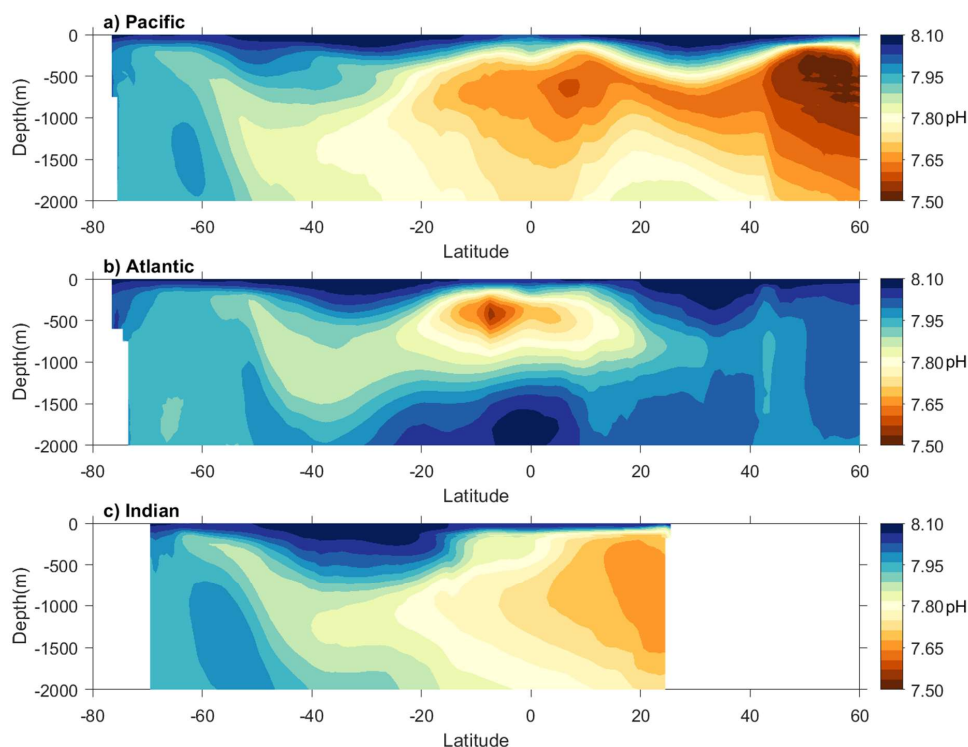
Figure 9: Climatological vertical distribution of zonal average FFNN pH in main basins.

3.2.2 Uncertainty

As described in the method section, the FFNN predicted pH was converted to $[H^+]$ to calculate the regional RMSE of $[H^+]$ between FFNN results and GLODAP measurements, and then the RMSE of $[H^+]$ in each SOM province was used to calculate the pH product uncertainty caused by the construction algorithm (Equation 2). Due to higher predicting errors, the pH product uncertainty is relatively higher near the surface (Figure 10). The uncertainty is generally lower than 0.02 at depths from 500 m to 2000 m, except for some regions near the SOM province and vertical boundary. Although we have used a cross-boundary method to improve the FFNN performance near the SOM and vertical boundary, there are still some discontinuity problems and relatively higher uncertainty. In addition, the equatorial and polar regions show an uncertainty higher than 0.04. This is because the FFNN performance tends to be worse in regions with the highest and lowest pH levels than in regions where pH values are near the average level. Especially in the Arctic Ocean, the pH measurements are much sparser leading to the highest predicting error and pH uncertainty. Therefore, the constructed pH product should be cautiously used in regional analysis near the boundaries or equatorial and polar regions.
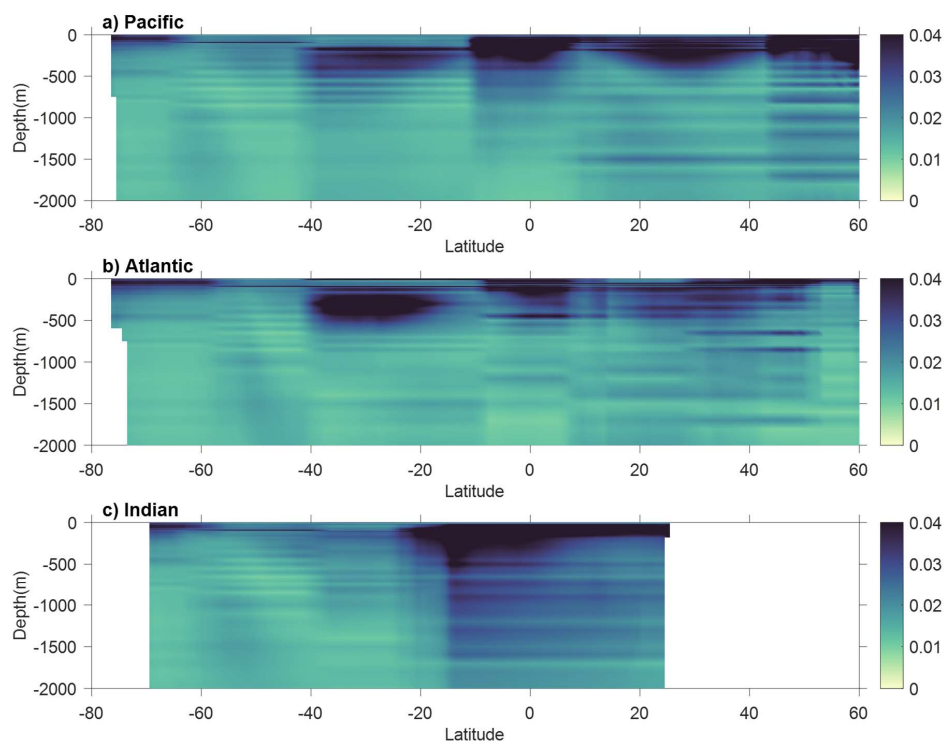
Figure 10: Uncertainty of FFNN pH product in main basins.

4 Data availability

335   The materials used in this research including the gridded seawater pH product (NetCDF files for all individual years), MATLAB code for construction and validation, and other materials (available as .m or .mat files) are available from the Marine Science Data Center of the Chinese Academy of Sciences at http://dx.doi.org/10.12157/IOCAS.20230720.001 (Zhong et al., 2023). The used pH measurements are available from GLODAP (https://glodap.info/index.php/merged-and-adjusted-data-product-v2-2023/, Lauvset et al., 2022), data products used for predictors are available from references listed in Table 1.

340   **5 Conclusions**

Quantifying the global seawater pH variability is important for understanding the future responses of oceans on the uptake of anthropogenic CO_2. A four-dimensional global seawater pH product covering depths from the surface to 2000 m and years from 1992 to 2020 was constructed in this work. The pH product brings insights into acidification research when observations are unavailable, but still should be used carefully in regional analyses. The analysis of pH RMSE and uncertainty suggested

345   that the constructed pH product remains limited in equatorial and polar regions and along the SOM boundary lines. This limitation was caused by sparse measurements and method disadvantages, which can be mitigated in future improvement works. Potential improvement may be achieved by increasing more predictor products to capture the pH drivers, testing more machine learning algorithms, and accumulating more seawater pH observations. Besides, the method used to construct the pH product can be applied in constructing global fields of other ocean chemical variables, such as nutrients,

350 particulate organic carbon, and dissolved inorganic carbon. The global field of these variables may further improve the pH product accuracy, as climatological products of these variables were used as pH predictors and lacked interannual variability information. Overall, decreasing seawater pH will influence the metabolism of marine organisms and result in notable changes to the marine ecosystem. The discrete observations may be insufficient to support research on large scales. With the machine learning method in this work, the discrete pH measurements were mapped to global gridded fields to fill the unsampled areas.

355 Our product can be used for analysis of seasonal to decadal and regional to global pH variability, to break through the limitation of discrete observations.

Acknowledgments

We thank the data support of the Marine Science Data Center and Public Technical Service Center, Institute of Oceanology, Chinese Academy of Sciences. We thank GLODAP for sharing the pH observation data. We thank the support

360 by the National Natural Science Foundation of China (grant nos.42176200); Laboratory for Marine Ecology and Environmental Science, Qingdao National Laboratory for Marine Science and Technology (LSKJ202204001, LSKJ202205001); National Key Research and Development Program (2022YFC3104305); Shandong Province and Yantai City Talent Programs; and Science Fund for Creative Research Groups of the National Natural Science Foundation of China (42221005).

365 **Author contributions:**

Data product collection: Baoxiao Qu, Yanjun Wang, Bin Zhang; Data product synthesize: Jun Ma, Qidong Wang, Jianwei Xing; Methodology: Guorong Zhong, Jiajia Dai, Liqin Duan, Ning Li; Model improve: Xuegang Li, Jinming Song, Huamao Yuan; Writing – original draft: Guorong Zhong, Xuegang Li; Writing – review & editing: Jinming Song, Fan Wang, Lijing Cheng.

370 **Competing interests:** Authors declare that they have no competing interests.

References

Bates, N. R. Interannual variability of the oceanic CO_2 sink in the subtropical gyre of the North Atlantic Ocean over the last 2 decades. Journal of Geophysical Research: Oceans, 112, C9, https://doi.org/10.1029/2006JC003759, 2007.

Bates, N. R., Astor, Y. M., Church, M. J., Currie, K., Dore, J. E., González-Dávila, M., ... & Santana-Casiano, J. M. A time-

375 series view of changing surface ocean chemistry due to ocean uptake of anthropogenic CO_2 and ocean acidification. Oceanography, 27, 126-141, https://doi.org/10.5670/oceanog.2014.16, 2014.

Bates, N. R., & Johnson, R. J. Acceleration of ocean warming, salinification, deoxygenation and acidification in the surface subtropical North Atlantic Ocean. Communications Earth & Environment, 1, 33, https://doi.org/10.1038/s43247-020-00030-5, 2020.

380 Broullón, D., Pérez, F. F., Velo, A., Hoppema, M., Olsen, A., Takahashi, T., ... & van Heuven, S. M. A global monthly climatology of total alkalinity: a neural network approach. Earth System Science Data, 11, 1109-1127, https://doi.org/10.5194/essd-11-1109-2019, 2019.

Broullón, D., Pérez, F. F., Velo, A., Hoppema, M., Olsen, A., Takahashi, T., ... & Kozyr, A. A global monthly climatology of oceanic total dissolved inorganic carbon: a neural network approach. Earth System Science Data, 12, 1725-1743,

385 https://doi.org/10.5194/essd-12-1725-2020, 2020.

Caldeira, K., & Wickett, M. E. Anthropogenic carbon and ocean pH. Nature, 425, 365-365, https://doi.org/10.1038/425365a, 2003.

Chau T T T, Gehlen M, Chevallier F. A seamless ensemble-based reconstruction of surface ocean pCO_2 and air–sea CO_2 fluxes over the global coastal and open oceans. Biogeosciences, 19, 1087-1109, https://doi.org/10.5194/bg-19-1087-2022, 2022.

390   Chen, C. T. A., Lui, H. K., Hsieh, C. H., Yanagi, T., Kosugi, N., Ishii, M., & Gong, G. C. Deep oceans may acidify faster than anticipated due to global warming. Nature Climate Change, 7, 890-894, https://doi.org/10.1038/s41558-017-0003-y, 2017.

Cheng, L., & Zhu, J. Benefits of CMIP5 multimodel ensemble in reconstructing historical ocean subsurface temperature variations. Journal of Climate, 29, 5393-5416, https://doi.org/10.1175/JCLI-D-15-0730.1, 2016.

Cheng, L., Trenberth, K. E., Fasullo, J., Boyer, T., Abraham, J., & Zhu, J. Improved estimates of ocean heat content from 1960
395   to 2015. Science Advances, 3, e1601545, https://doi.org/10.1126/sciadv.1601545, 2017.

Cheng, L., Trenberth, K. E., Gruber, N., Abraham, J. P., Fasullo, J. T., Li, G., ... & Zhu, J. Improved estimates of changes in upper ocean salinity and the hydrological cycle. Journal of Climate, 33, 10357-10381, https://doi.org/10.1175/JCLI-D-20-0366.1, 2020.

Climate Prediction Center. Daily Arctic Oscillation Index. [Accessed on 2023/08/20].
400   https://www.cpc.ncep.noaa.gov/products/precip/CWlink/daily_ao_index/ao_index.html. (2002).

Climate Prediction Center. Southern Oscillation Index. [Accessed on 2023/08/20]. https://www.cpc.ncep.noaa.gov/products/analysis_monitoring/ensocycle/soi.shtml. (2005).

Dore, J. E., Lukas, R., Sadler, D. W., Church, M. J., & Karl, D. M. Physical and biogeochemical modulation of ocean acidification in the central North Pacific. Proceedings of the National Academy of Sciences, 106, 12235-12240,
405   https://doi.org/10.1073/pnas.0906044106, 2009.

Fay, A. R., & McKinley, G. A. Global trends in surface ocean pCO_2 from in situ data. Global Biogeochemical Cycles, 27, 541-557, https://doi.org/10.1002/gbc.20051, 2013.

Feely, R. A., Sabine, C. L., Lee, K., Berelson, W., Kleypas, J., Fabry, V. J., & Millero, F. J. Impact of anthropogenic CO_2 on the $CaCO_3$ system in the oceans. Science, 305, 362-366, https://doi.org/10.1126/science.1097329, 2004.

410   Feely, R. A., Doney, S. C., & Cooley, S. R. Ocean acidification: Present conditions and future changes in a high-CO_2 world. Oceanography, 22, 36-47, https://doi.org/10.5670/oceanog.2009.95, 2009.

Friedlingstein, P., O'sullivan, M., Jones, M. W., Andrew, R. M., Bakker, D. C., Hauck, J., ... & Zheng, B. Global carbon budget 2023. Earth System Science Data, 15(12), 5301-5369, https://doi.org/10.5194/essd-15-5301-2023, 2023.

Garcia He, Weathers Kw, Paver Cr, Smolyar I, Boyer Tp, Locarnini Mm, Zweng Mm, Mishonov Av, Baranova Ok, Seidov
415   D, Reagan Jr. World Ocean Atlas 2018, Volume 3: Dissolved Oxygen, Apparent Oxygen Utilization, and Dissolved Oxygen Saturation. NOAA Atlas NESDIS 83, 38pp, https://archimer.ifremer.fr/doc/00651/76337/, 2019a.

Garcia He, Weathers Kw, Paver Cr, Smolyar I, Boyer Tp, Locarnini Mm, Zweng Mm, Mishonov Av, Baranova Ok, Seidov D, Reagan Jr. World Ocean Atlas 2018. Vol. 4: Dissolved Inorganic Nutrients (phosphate, nitrate and nitrate+nitrite, silicate). NOAA Atlas NESDIS 84, 35pp, https://archimer.ifremer.fr/doc/00651/76336/, 2019b.

420   GEBCO Compilation Group. GEBCO_2022 Grid. [Accessed on 2022/12/01]. https://www.gebco.net/data_and_products/gridded_bathymetry_data/#global, 2022.

González-Dávila, M., Santana-Casiano, J. M., Rueda, M. J., & Llinás, O. The water column distribution of carbonate system variables at the ESTOC site from 1995 to 2004. Biogeosciences, 7, 3067–3081, https://doi.org/10.5194/bg-7-3067-2010, 2010.

Guallart, E. F., Fajar, N. M., Padín, X. A., Vázquez-Rodríguez, M., Calvo, E., Ríos, A. F., ... & Pérez, F. F. Ocean acidification
425   along the 24.5° N section in the subtropical North Atlantic. Geophysical Research Letters, 42, 450-458, https://doi.org/10.1002/2014gl062971, 2015.

Hersbach, H., Bell, B., Berrisford, P., Hirahara, S., Horányi, A., Muñoz-Sabater, J., ... & Thépaut, J. N. The ERA5 global reanalysis. Quarterly Journal of the Royal Meteorological Society, 146(730), 1999-2049, https://doi.org/10.1002/qj.3803, 2020.

430   Iida, Y., Takatani, Y., Kojima, A., & Ishii, M. Global trends of ocean CO_2 sink and ocean acidification: an observation-based reconstruction of surface ocean inorganic carbon variables. Journal of Oceanography, 77, 323-358, https://doi.org/10.1007/s10872-020-00571-5, 2021.

Ishizu, M., Miyazawa, Y., & Guo, X. Long-term variations in ocean acidification indices in the Northwest Pacific from 1993 to 2018. Climatic Change, 168, 1-20, https://doi.org/10.1007/s10584-021-03239-1, 2021.

435 Lan, X., Tans, P. & K.W. Thoning. Trends in globally-averaged CO_2 determined from NOAA Global Monitoring Laboratory measurements. https://gml.noaa.gov/ccgg/trends/, 2023.

Landschützer, P., Gruber, N., Bakker, D. C., & Schuster, U. Recent variability of the global ocean carbon sink. Global Biogeochemical Cycles, 28(9), 927-949, https://doi.org/10.1002/2014gb004853, 2014.

Landschützer, P., Laruelle, G. G., Roobaert, A., & Regnier, P. A uniform pCO_2 climatology combining open and coastal

440 oceans. Earth System Science Data, 12, 2537-2553, https://doi.org/10.5194/essd-2020-90, 2020.

Lauvset, S. K., Gruber, N., Landschützer, P., Olsen, A., & Tjiputra, J. Trends and drivers in global surface ocean pH over the past 3 decades. Biogeosciences, 12, 1285-1298, https://doi.org/10.5194/bg-12-1285-2015, 2015.

Lauvset, S. K., Key, R. M., Olsen, A., Van Heuven, S., Velo, A., Lin, X., ... & Watelet, S. A new global interior ocean mapped climatology: The 1× 1 GLODAP version 2. Earth System Science Data, 8, 325-340, https://doi.org/10.5194/essd-8-325-2016

445 , 2016.

Lauvset, S. K., Carter, B. R., Pérez, F. F., Jiang, L. Q., Feely, R. A., Velo, A., & Olsen, A. Processes driving global interior ocean pH distribution. Global Biogeochemical Cycles, 34(1), e2019GB006229, https://doi.org/10.1029/2019gb006229, 2020.

Lauvset, S. K., Lange, N., Tanhua, T., Bittig, H. C., Olsen, A., Kozyr, A., ... & Key, R. M. GLODAPv2. 2022: the latest version of the global interior ocean biogeochemical data product. Earth System Science Data, 14, 5543-5572,

450 https://doi.org/10.5194/essd-14-5543-2022, 2022.

Le Quéré, C., Takahashi, T., Buitenhuis, E. T., Rödenbeck, C., & Sutherland, S. C. Impact of climate change and variability on the global oceanic sink of CO_2. Global Biogeochemical Cycles, 24, 4, https://doi.org/10.1029/2009GB003599, 2010.

Lewis, E., Wallace, D., & Allison, L. J. (1998). Program developed for CO_2 system calculations (No. ORNL/CDIAC-105). Brookhaven National Lab., Dept. of Applied Science, Upton, NY (United States); Oak Ridge National Lab., Carbon Dioxide

455 Information Analysis Center, TN (United States).

Li, L., Chen, B., Luo, Y., Xia, J., & Qi, D. Factors controlling acidification in intermediate and deep/bottom layers of the Japan/East Sea. Journal of Geophysical Research: Oceans, 127, e2021JC017712, https://doi.org/10.1029/2021jc017712, 2022.

Luo, Y., Boudreau, B. P., & Mucci, A. Disparate acidification and calcium carbonate desaturation of deep and shallow waters of the Arctic Ocean. Nature Communications, 7, 12821, https://doi.org/10.1038/ncomms12821, 2016.

460 Menemenlis, D., Campin, J. M., Heimbach, P., Hill, C., Lee, T., Nguyen, A., ... & Zhang, H. ECCO2: High resolution global ocean and sea ice data synthesis. Mercator Ocean Quarterly Newsletter, 31, 13-21, https://doi.org/, 2008.

NASA Ocean Biology Processing Group. Aqua MODIS Level 3 Mapped Chlorophyll Data, Version R2022.0 [dataset]. NASA Ocean Biology Distributed Active Archive Center. https://doi.org/10.5067/AQUA/MODIS/L3M/CHL/2022, 2022.

NASA Ocean Biology Processing Group. Aqua MODIS Level 3 Mapped Downwelling Diffuse Attenuation Coefficient Data,

465 Version R2022.0 [dataset]. NASA Ocean Biology Distributed Active Archive Center. https://doi.org/10.5067/AQUA/MODIS/L3M/KD/2022, 2022.

NASA Ocean Biology Processing Group. Aqua MODIS Level 3 Mapped Inherent Optical Properties Data, Version R2022.0 [dataset]. NASA Ocean Biology Distributed Active Archive Center. https://doi.org/10.5067/AQUA/MODIS/L3M/IOP/2022, 2022.

470 NASA Ocean Biology Processing Group. Aqua MODIS Level 3 Mapped Photosynthetically Available Radiation Data, Version R2022.0 [dataset]. NASA Ocean Biology Distributed Active Archive Center. https://doi.org/10.5067/AQUA/MODIS/L3M/PAR/2022, 2022.

NASA Ocean Biology Processing Group. Aqua MODIS Level 3 Mapped Particulate Organic Carbon Data, Version R2022.0 [dataset]. NASA Ocean Biology Distributed Active Archive Center. https://doi.org/10.5067/AQUA/MODIS/L3M/POC/2022,

475 2022.

Orr, J. C., Fabry, V. J., Aumont, O., Bopp, L., Doney, S. C., Feely, R. A., ... & Yool, A. Anthropogenic ocean acidification over the twenty-first century and its impact on calcifying organisms. Nature, 437, 681-686, https://doi.org/10.1038/nature04095, 2005.

Qi, D., Ouyang, Z., Chen, L., Wu, Y., Lei, R., Chen, B., ... & Cai, W. J. Climate change drives rapid decadal acidification in
480   the Arctic Ocean from 1994 to 2020. Science, 377, 1544-1550, https://doi.org/10.1126/science.abo0383, 2022.

Sabine, C. L., & Tanhua, T. Estimation of anthropogenic CO_2 inventories in the ocean. Annual Review of Marine Science, 2, 175-198, https://doi.org/10.1146/annurev-marine-120308-080947, 2010.

Takahashi, T., Sutherland, S. C., Chipman, D. W., Goddard, J. G., Ho, C., Newberger, T., ... & Munro, D. R. Climatological distributions of pH, pCO_2, total CO_2, alkalinity, and $CaCO_3$ saturation in the global surface ocean, and temporal changes at
485   selected locations. Marine Chemistry, 164, 95-125, https://doi.org/10.1016/j.marchem.2014.06.004, 2014.

Terhaar, J., Kwiatkowski, L., & Bopp, L. Emergent constraint on Arctic Ocean acidification in the twenty-first century. Nature, 582, 379-383, https://doi.org/10.1038/s41586-020-2360-3, 2020.

Wolter, K., & Timlin, M. S. El Niño/Southern Oscillation behaviour since 1871 as diagnosed in an extended multivariate ENSO index (MEI. ext). International Journal of Climatology, 31, 1074-1087, https://doi.org/10.1002/joc.2336, 2011.

490   Zhong, G., Li, X., Song, J., Qu, B., Wang, F., Wang, Y., ... & Duan, L. Reconstruction of global surface ocean pCO_2 using region-specific predictors based on a stepwise FFNN regression algorithm. Biogeosciences, 19, 845-859, https://doi.org/10.5194/bg-19-845-2022, 2022.

Zhong, G; Li, X., Song, J. Global ocean gridded seawater pH during 1992-2020 at 0-2000 m depth based on Stepwise FFNN algorithm 2023 version. Marine Science Data Center of the Chinese Academy of Sciences
495   (http://dx.doi.org/10.12157/IOCAS.20230720.001), 2023